

1      **From typhoon rainfall to slope failure: optimizing susceptibility**  
2      **models and dynamic thresholds for landslide warnings in Zixing**  
3      **City, China**

4      **Weifeng Xiao<sup>1</sup>, Guangchong Yao<sup>1</sup>, Zhenghui Xiao<sup>1</sup>, Ge Liu<sup>\*2</sup>, Luguang Luo<sup>1</sup>, Yunjiang**  
5      **Cao<sup>1</sup>, Wei Yin<sup>3</sup>**

6

7      <sup>1</sup>School of Earth Sciences and Spatial Information Engineering, Hunan University of Science and  
8      Technology, Xiangtan 411201, China

9      <sup>2</sup>Northeast Institute of Geography and Agroecology, CAS, Changchun 130102, China

10     <sup>3</sup>Hunan Institute of Geological Disaster Investigation and Monitoring, Changsha 410004, China

11

12     Corresponding author.

13     E-mail address: liuge@iga.ac.cn (Ge Liu)

14     **Abstract:** Typhoon-specific rainfall-induced landslides present a severe threat in  
15     mountainous regions. Existing warning systems, however, often fail to account for the distinct  
16     rainfall dynamics of these extreme events. To bridge this gap, an integrated framework is  
17     proposed, combining optimized susceptibility predictions with dynamic rainfall thresholds  
18     tailored to typhoon patterns. The approach enhances machine learning accuracy through  
19     buffer-based negative sampling and variable weighting. It also introduces a spatiotemporal  
20     rainfall analysis to distinguish between short-term intense downpours and cumulative soil  
21     saturation. Tested in Zixing City, Hunan Province, China, following over 700 landslides  
22     triggered by Typhoon Gaemi, the framework proved its effectiveness. Support Vector  
23     Machine (SVM) models with frequency ratio (FR) inputs yielded the highest accuracy in  
24     predicting these slope failures. Rainfall analysis identified the combination of 24-hour  
25     intensity and 7-day antecedent rainfall as the optimal trigger. This pairing effectively captures  
26     both immediate and cumulative moisture effects. Spatially, granite slopes and areas near roads  
27     emerged as critical hotspots for failure. Ultimately, the framework generates high-risk zone

28 maps that align strongly with historical events. This work underscores the unique nature of  
29 typhoon-driven slope instability and offers a transferable framework for disaster risk  
30 reduction in cyclone-prone regions.

31 **Keywords:** Typhoon-induced landslide; Slope failure; Hazard warning system; Dynamic  
32 thresholds; Landslide susceptibility mapping

33 **1 Introduction**

34 Landslides pose significant threats to mountainous regions globally (Froude and Petley,  
35 2018), especially in areas where steep terrain, complex geology (Thiene et al., 2017), and  
36 extreme weather events like typhoons intersect. In Southeast China, typhoon-induced  
37 landslides have become a growing concern due to the region's rapid urbanization and the  
38 increasing variability in climate patterns (Gariano and Guzzetti, 2016; Fan et al., 2018). The  
39 Nanling Mountains, in southern China, are particularly vulnerable to landslides due to a  
40 combination of extreme topographic relief and complex geological conditions during the  
41 typhoon season (Zou et al., 2023).

42 Typhoons typically bring prolonged antecedent rainfall, followed by intense, short bursts  
43 of precipitation (Li et al., 2019). These conditions create unique hydrological environments  
44 that exceed the complexity of typical rainfall-triggered landslides (Chung and Li, 2022).  
45 These events trigger slope failures through cumulative soil saturation and sudden hydrological  
46 stress, challenging traditional landslide prediction methods (Yang et al., 2017). Despite  
47 advances in landslide susceptibility prediction (LSP) and rainfall threshold modeling, current  
48 approaches remain inadequate. Three critical limitations persist: severe data imbalance effects,  
49 suboptimal integration of variable selection with machine learning algorithms, and lack of  
50 spatially-explicit rainfall thresholds for typhoon-specific conditions (Segoni et al., 2018a;  
51 Regmi et al., 2024).

52        Most existing studies employ ad-hoc buffer distances without systematic optimization,  
53        leading to inconsistent model performance across different geological settings (Lombardo and  
54        Mai, 2018). Traditional methods attempt to mitigate this imbalance by randomly sampling  
55        non-landslide points across the study area (Steger et al., 2016; Dou et al., 2023). However,  
56        random selection can introduce spatial bias, as non-landslide points might include areas that  
57        are unstable but have not yet been identified as landslide-prone (Kalantar et al., 2018).

58        To address this limitation, more recent approaches have employed buffer-based negative  
59        sampling, which systematically excludes non-landslide points near known landslide sites.  
60        This method assumes that adjacent areas share similar environmental conditions (e.g., slope,  
61        lithology) and therefore should not be classified as “stable” (Achu et al., 2022). Several  
62        studies have tested varying buffer distances, ranging from tens to thousands of meters, to  
63        determine the optimal distance for different regions. However, systematic evaluation of buffer  
64        distance optimization coupled with variable weighting methods remains largely unexplored.

65        LSP is primarily focused on identifying areas prone to slope failure, based on static  
66        environmental factors such as topography, lithology, land cover, and hydrology (Zêzere et al.,  
67        2017; Guo et al., 2024). Traditional approaches to LSP often rely on deterministic and  
68        statistical methods, including information value (IV), certainty factor (CF), frequency ratio  
69        (FR), logistic regression (LR), and weight of evidence (WOE). These methods quantify the  
70        relationship between historical landslide occurrences and predisposing factors using linear or  
71        semi-linear approaches (Ciurleo et al., 2017; Reichenbach et al., 2018). However, these  
72        methods oversimplify the complex, nonlinear interactions that govern slope stability  
73        (Merghadi et al., 2020).

74        In contrast, machine learning (ML) algorithms, such as support vector machine (SVM)  
75        and light gradient boosting machine (LightGBM), have emerged as powerful alternatives.  
76        SVM excels in high-dimensional classification tasks and effectively identifies optimal

77 hyperplanes separating landslide-prone from stable areas (San, 2014; Huang and Zhao, 2018).  
78 LightGBM offers superior scalability and computational efficiency for processing large  
79 geospatial datasets (Sun et al., 2023). Both SVM and LightGBM capture intricate  
80 relationships among variables without restrictive assumptions, making them superior to  
81 traditional methods in terms of predictive accuracy (Yang et al., 2023). However, frameworks  
82 that systematically integrates variable weighting methods with advanced ML algorithms for  
83 LSP optimization are lacking.

84 For temporal prediction, existing rainfall threshold approaches predominantly use  
85 generalized regional thresholds that inadequately capture local geological heterogeneity and  
86 typhoon-specific rainfall patterns (Guzzetti, 2021; Banfi and De Michele, 2024). These  
87 thresholds are typically defined based on cumulative or intensity-duration (I-D) rainfall values  
88 (Piciullo et al., 2017; Segoni et al., 2018a). In typhoon-prone regions, dynamic rainfall  
89 thresholds are crucial due to the unique combination of long-duration antecedent rainfall and  
90 sudden high-intensity bursts of precipitation (Guzzetti et al., 2020). Traditional empirical  
91 methods fail to provide spatially continuous threshold surfaces that account for local  
92 environmental variability (Piciullo et al., 2018).

93 Recent advances have integrated multi-temporal rainfall parameters with advanced  
94 statistical techniques to optimize rainfall thresholds (Segoni et al., 2015; Huang et al., 2022),  
95 accounting for diverse triggering mechanisms. Additionally, spatial interpolation methods,  
96 such as Kriging, have been applied to generate continuous rainfall threshold surfaces that  
97 allow for local variations in geological and environmental conditions (Kenanoglu et al., 2019;  
98 Segoni et al., 2018b). This approach, when combined with high-resolution susceptibility maps,  
99 contributes to the development of integrated hazard warning systems that can dynamically  
100 adjust to typhoon-specific rainfall-induced scenarios (Piciullo et al., 2018; Mirus et al., 2018).

101 This study examines Zixing City, a mountainous region in southeastern Hunan Province,  
102 frequently affected by typhoon-induced extreme rainfall. Its steep slopes, fractured geology,  
103 and high sensitivity to rapid pore-pressure increase render it particularly vulnerable (Ma et al.,  
104 2025). The large number of landslides (>700) triggered by Typhoon Gaemi in July 2024  
105 provides a valuable dataset for model calibration and validation.

106 Here we developed an integrated framework that combines (i) optimised buffer distances  
107 for negative sampling, (ii) bivariate weighting methods (IV, CF, FR) with advanced machine  
108 learning classifiers (SVM, LightGBM), and (iii) spatially continuous, typhoon-specific  
109 rainfall thresholds derived through Kriging interpolation. The specific objectives are to (1)  
110 determine optimal buffer distances that minimise spatial bias in imbalanced datasets, (2)  
111 evaluate the performance gain from coupling bivariate weights with machine learning  
112 algorithms, (3) establish dynamic rainfall thresholds suited to typhoon rainfall patterns, (4)  
113 generate continuous threshold surfaces via Kriging, and (5) integrate high-resolution  
114 susceptibility maps with these thresholds to support an operational early warning system. This  
115 approach improves landslide prediction in typhoon-prone mountainous regions and provides a  
116 transferable methodology for similar environments.

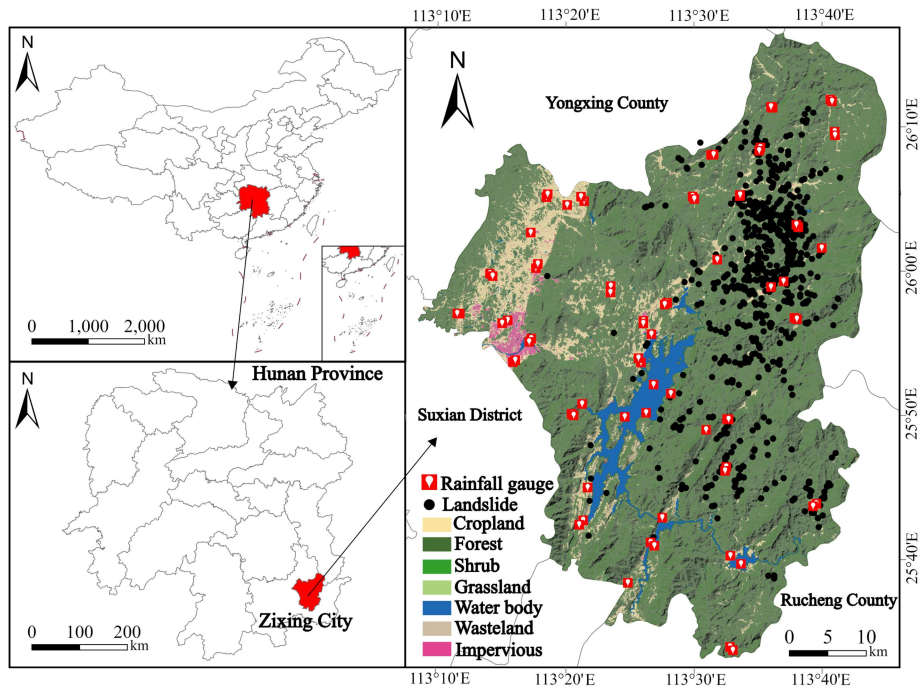
## 117 **2 Study area and data sources**

### 118 **2.1 Study area**

119 Zixing City ( $25^{\circ}34'–26^{\circ}18' \text{ N}$ ,  $113^{\circ}08'–113^{\circ}44' \text{ E}$ ), covering  $2,747 \text{ km}^2$  in southeastern  
120 Hunan Province, China (Fig. 1), is located within the Nanling Mountains geological province.  
121 Situated approximately 400 km inland from the South China Sea, Zixing lies at the  
122 intersection of the Nanling Mountains and low hills, forming a watershed divide between the  
123 Yangtze and Pearl River basins. The region is characterized by steep topography, with  
124 elevations ranging from 125 to 1,691 meters and slopes exceeding  $30^{\circ}$  across 78% of the area.  
125 This mountainous terrain, combined with fractured geology and active NE-SW trending faults

126 such as the Chaling-Yongxing Fault Zone, creates a permeable fracture network that  
127 facilitates groundwater drainage.

128 The climate of Zixing is subtropical monsoon, with annual precipitation averaging 1,550  
129 mm, 70% of which occurs from April to September. Typhoons significantly contribute to  
130 rainfall, inducing rapid pore-pressure increases in shallow aquifers (3–8 m depth). These  
131 climatic and geological conditions make Zixing particularly vulnerable to landslides,  
132 providing a valuable context for this study. The extensive landslide dataset triggered by  
133 Typhoon Gaemi in July 2024 (>700 events) serves as a critical resource for model calibration  
134 and validation.



135  
136 **Figure 1** Geographical distribution of the study area, landslides and rainfall gauges.

## 137 **2.2 Data collection and preprocessing**

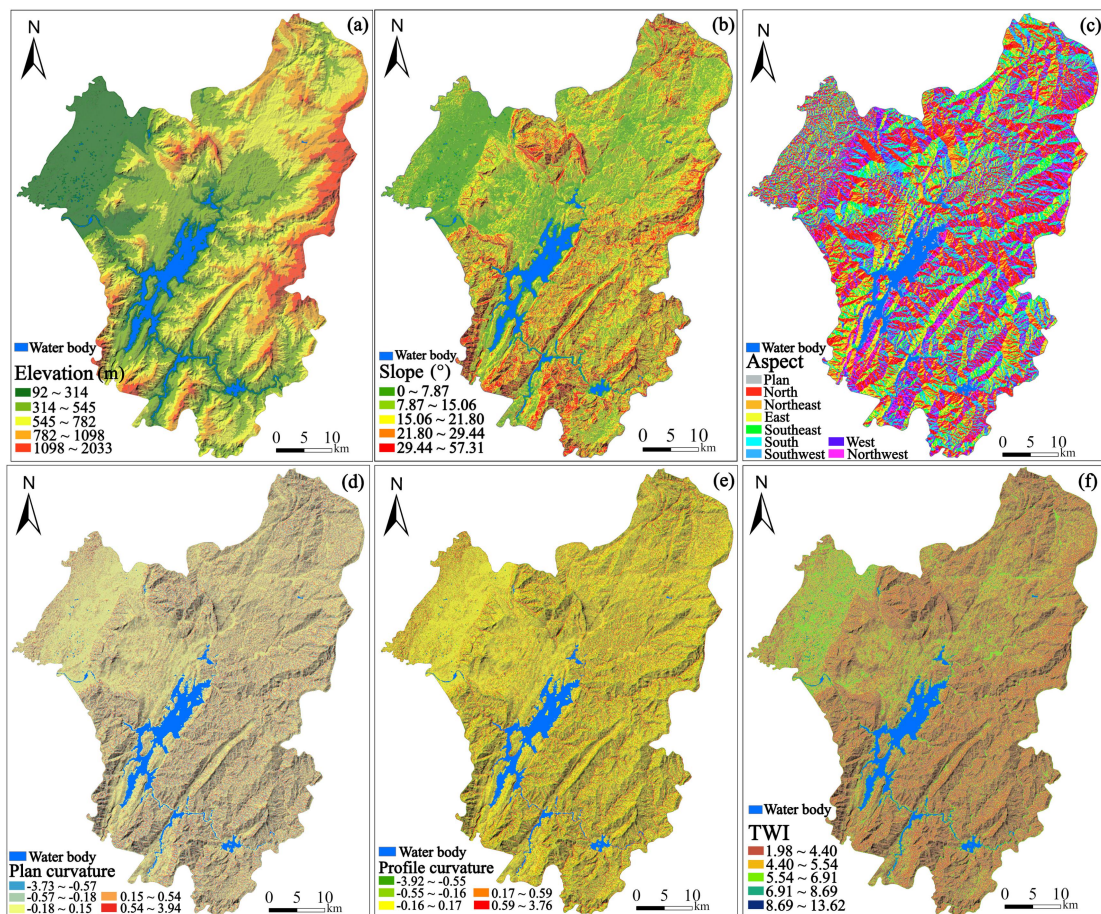
### 138 **2.2.1 Compilation of landslide catalogue**

139 A comprehensive inventory of 705 landslide events triggered by Typhoon Gaemi on July  
140 27, 2024, was compiled from the Hunan Center for Natural Resources Affairs. The landslide  
141 locations were verified through field inspections and high-resolution satellite imagery to  
142 ensure spatial accuracy and completeness of the dataset.

143        **2.2.2 Landslides conditioning factors and data sources**

144        Based on extensive literature reviews and the geoenvironmental characteristics of the  
145        study area, twelve conditioning factors were selected for landslide susceptibility analysis:  
146        elevation, slope gradient, slope orientation, curvature, topographic wetness index (TWI),  
147        stream power index (SPI), normalized difference vegetation index (NDVI), distances to roads,  
148        rivers, and faults, and lithology (Fig. 2).

149        Topographic factors (elevation, slope gradient, slope orientation, TWI, SPI, and  
150        curvature) were extracted from a 30-meter digital elevation model (DEM) obtained from the  
151        Geospatial Data Cloud (<https://www.gscloud.cn>). Environmental factors including NDVI and  
152        proximity variables (distances to roads, rivers, and fault lines) were derived from 1:50,000-  
153        scale cartographic maps and Landsat 8 OLI imagery from the same platform. Geological  
154        composition and structural data were acquired from 1:100,000-scale geological maps.



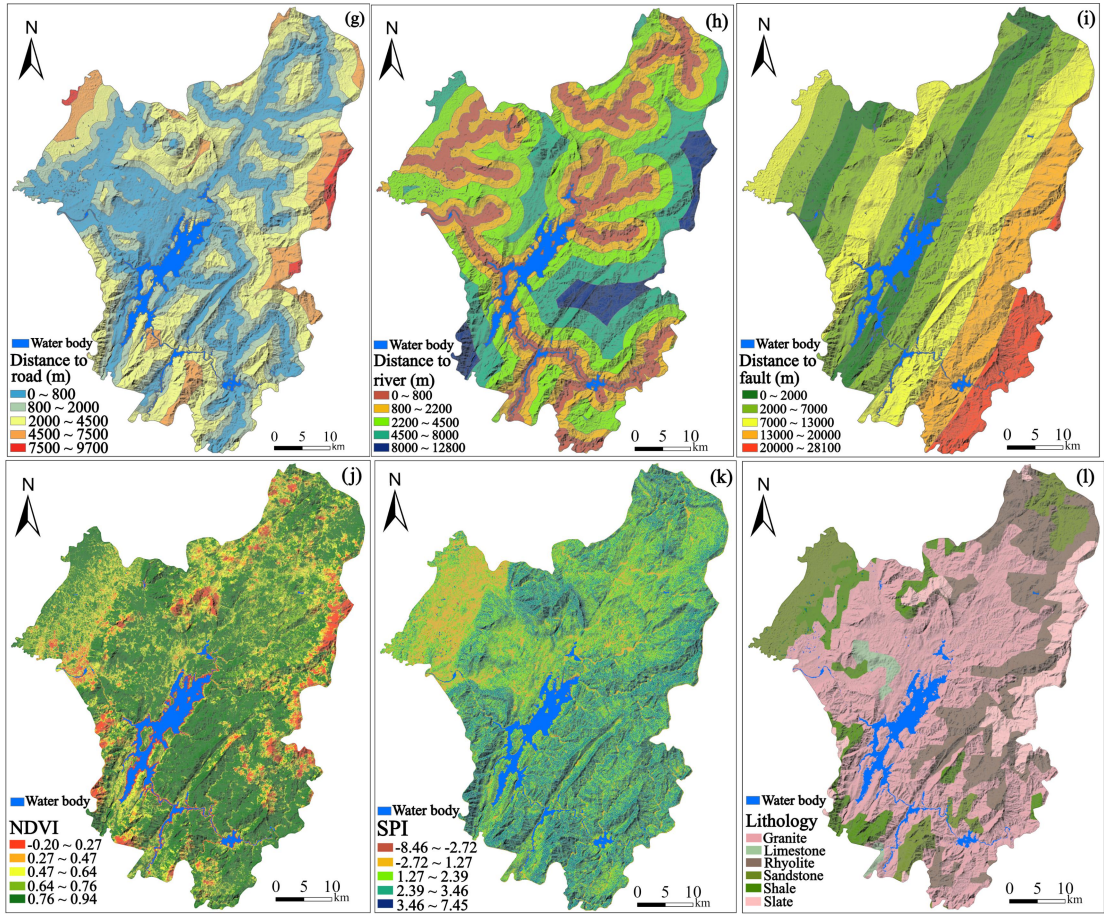


Figure 2 Landslide-related conditioning factors.

### 2.2.3 Data preprocessing and spatial standardization

We transformed all conditioning factors into continuous statistical measures using IV, CF, and FR methods and then resampled them to a uniform 60-meter resolution. This resolution was selected to balance computational efficiency with scale appropriateness for regional landslide analysis while maintaining compatibility with the available geological map scale (1:100,000).

The study area was divided into  $60 \times 60$  meter grid cells, with landslides smaller than the grid resolution aggregated to the nearest cell centroid. Multiple landslides within a single cell were treated as one event to maintain spatial independence required for machine learning modeling. This preprocessing approach ensures statistical validity by minimizing spatial autocorrelation effects while providing adequate representation of landslide distribution patterns across the study area.

172        **2.2.4 Rainfall data collection and spatial distribution**

173        Rainfall data for the study were obtained from 12 automatic rain gauge stations  
174        strategically distributed across Zixing City and its surrounding areas (Fig. 1). These stations,  
175        operated by the Hunan Meteorological Administration, provided hourly precipitation records  
176        during Typhoon Gaemi (July 20-30, 2024) and the preceding antecedent period. The spatial  
177        distribution of gauge stations ensured adequate coverage of the study area's topographic and  
178        climatic gradients.

179        To assign rainfall parameters (H1, H12, H24, H72, and D7) to each of the 705 landslide  
180        points, we employed the Kriging interpolation to generate spatially continuous rainfall  
181        surfaces from discrete gauge measurements. This geostatistical method accounts for spatial  
182        autocorrelation in rainfall patterns and provides optimal unbiased estimates by weighting  
183        nearby observations based on their spatial proximity and correlation structure.

184        Spherical variogram models were fitted to the rainfall data through iterative optimization,  
185        with model selection based on minimum Akaike Information Criterion (AIC) values. The  
186        interpolation accuracy was rigorously evaluated through leave-one-out cross-validation,  
187        where each gauge station was sequentially removed and its rainfall values predicted using the  
188        remaining 11 stations. Four statistical metrics were used to assess performance: Root Mean  
189        Square Error (RMSE), Mean Absolute Error (MAE), correlation coefficient (R), and Nash-  
190        Sutcliffe Efficiency (NSE).

191        **Table 1** Kriging interpolation accuracy assessment for rainfall parameters.

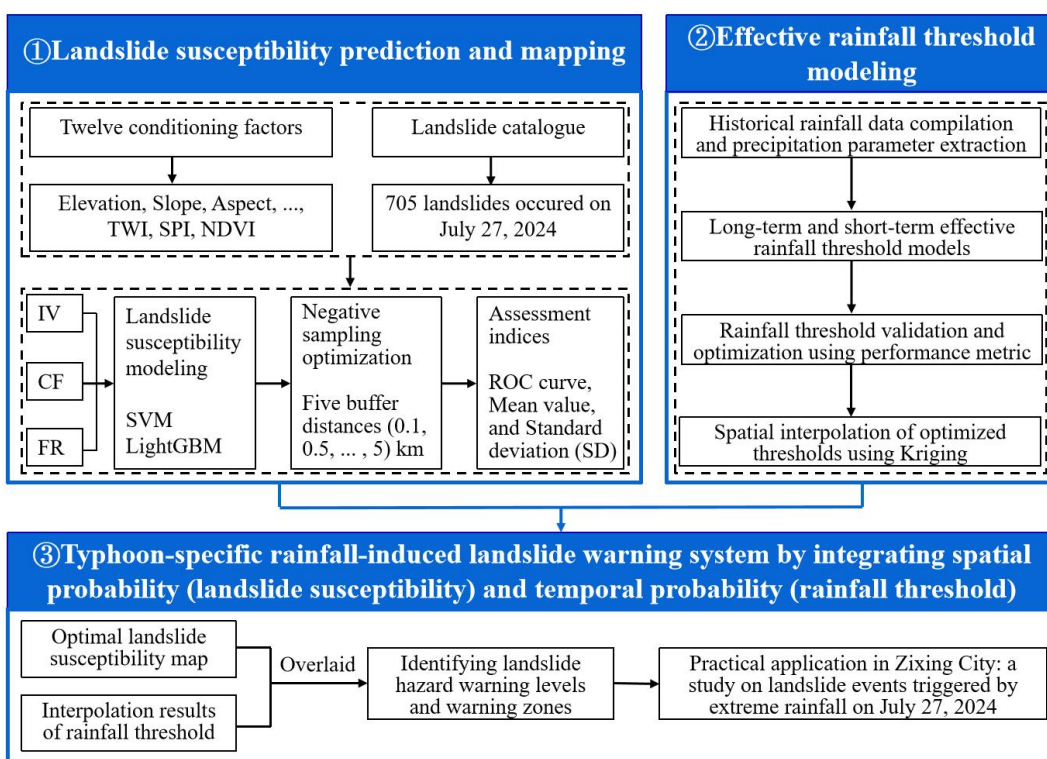
Parameter	RMSE (mm)	MAE	R	NSE
H1	4.2	3.1	0.76	0.71
H12	11.7	8.9	0.83	0.78
H24	16.3	12.6	0.87	0.82
H72	24.8	18.4	0.81	0.77
D7	29.6	22.7	0.78	0.73

192        The validation results demonstrated acceptable interpolation accuracy across all rainfall  
193        parameters, with correlation coefficients ranging from 0.76 to 0.87 and Nash-Sutcliffe

194 Efficiency values between 0.71-0.82. Despite some limitations inherent to the sparse gauge  
 195 network in mountainous terrain, the interpolation performance was deemed sufficient for  
 196 regional landslide susceptibility analysis, ensuring reasonable spatial representation of  
 197 precipitation patterns across the study area.

198 **3 Methodologies**

199 This study proposes an integrated framework for optimizing LSP and typhoon-specific  
 200 rainfall thresholds within hazard warning systems (Fig. 3). The framework includes the  
 201 following key components: (1) landslide susceptibility prediction and mapping, utilizing  
 202 twelve conditioning factors prioritizing typhoon-induced hydrological responses (e.g., TWI,  
 203 SPI) and 705 landslide records from July 27, 2024, optimized with five buffer distances and  
 204 evaluated using ROC curves; (2) dynamic rainfall threshold modeling based on typhoon  
 205 rainfall parameterization, validated and spatially interpolated using Kriging; and (3) the  
 206 integration of spatial and temporal probabilities to develop a **typhoon-specific rainfall-induced**  
 207 **landslide warning system**, demonstrated through a case study in Zixing City.



208

209 **Figure 3** Technical framework for developing a **typhoon-specific rainfall-induced landslide warning system**.

210        **3.1 Landslide susceptibility prediction and mapping**

211        **3.1.1 Machine learning models**

212        SVM is a robust supervised learning algorithm widely used for classification in landslide  
213        susceptibility mapping (Kalantar et al., 2018; Wang et al., 2020). For typhoon-triggered  
214        landslides, SVM effectively handles imbalanced datasets caused by concentrated slope  
215        failures in high-intensity rainfall zones. The SVM optimization problem is defined as:

216        
$$\min_{w,b,\xi} \frac{1}{2} w^T w + C \sum_{i=1}^n \xi_i \quad (1)$$

217        subject to the constraint:

218        
$$y_i (w^T \phi(x_i) + b) \geq 1 - \xi_i, \quad \xi_i \geq 0, \quad i = 1, \dots, n \quad (2)$$

219        where  $w$  is the normal vector to the hyperplane,  $b$  is the bias term,  $\xi_i$  are slack variables,  $C$  is  
220        the regularization parameter, and  $\phi(x_i)$  maps input vectors to a higher-dimensional space. The  
221        variable  $y_i$  represents the class label (-1 or 1) for each sample  $x_i$ .

222        LightGBM is an efficient gradient boosting framework for large datasets, known for  
223        training an ensemble of decision trees by iteratively adding trees that minimize errors from  
224        previous trees. LightGBM's scalability is critical for processing typhoon-related geospatial  
225        data (e.g., hourly rainfall grids) across 2,746 km<sup>2</sup> (Sun et al., 2023; Sahin, 2020). The  
226        minimized objective function is expressed as:

227        
$$L = \sum_{i=1}^N (y_i - \hat{y}_i)^2 + \lambda \sum_{j=1}^M \|\theta_j\|^2 \quad (3)$$

228        where  $y_i$  is the true label,  $\hat{y}_i$  is the predictive value,  $\lambda$  is a regularization parameter, and  
229         $\theta_j$  represents the parameters of the model.

230        **3.1.2 Input variable weighting methods**

231        The IV method, grounded in information theory, assesses how different factors  
232        contribute to landslide susceptibility within a study area (Niu et al., 2024). Factors such as

233 distance to roads and lithology were weighted higher in Zixing City due to their interaction  
 234 with typhoon-induced soil saturation. The IV for each evaluation factor is determined using  
 235 the formula below:

$$236 \quad IV(F_i, K) = \ln \frac{N_i / N}{S_i / S} \quad (4)$$

237 where  $IV(F_i, K)$  is the information value of evaluation factor  $F_i$  in relation to landslide event  $K$ ,  
 238  $N_i$  refers to the number of landslides,  $N$  is the total number of landslides,  $S_i$  represents the area  
 239 covered by factor  $F_i$ , and  $S$  is the total area of the study area.

240 The CF **method** is a widely utilized probabilistic technique for assessing the likelihood of  
 241 landslide **occurrences** (Zhao et al., 2021). It quantifies the prior probability of a landslide  
 242 **initiation under specific conditions of influential factors, utilizing spatial data from known**  
 243 **landslide locations**. The expression of CF is as follows:

$$244 \quad CF = \begin{cases} \frac{PP_a - PP_s}{PP_s(1-PP_a)}, & PP_a < PP_s \\ \frac{PP_a - PP_s}{PP_a(1-PP_s)}, & PP_a \geq PP_s \end{cases} \quad (5)$$

245 where **CF** is the certainty factor indicating the degree of association between an influential  
 246 factor and potential landslide occurrence. It is derived from two area-proportional measures:  
 247  $PP_a$ , the proportion of landslide points within a specific factor class (number of landslide  
 248 points in the class / total area of the class); and  $PP_s$ , the proportion of landslide points across  
 249 the entire study region (total number of landslide points / total area of the region).

250 The FR is a prevalent method in statistical analysis that assesses the relative impact of  
 251 various factors on the incidence of landslides (Panchal et al., 2021). An elevated FR value  
 252 denotes a more significant influence of a factor on the likelihood of landslides. The FR is  
 253 determined by the following equation:

$$254 \quad FR = \frac{N_i / N}{S_i / S} \quad (6)$$

255 where  $FR$  is the frequency ratio,  $N_i$  represents the account of landslides within the area  
256 corresponding to the conditioning factor,  $N$  is the total number of landslides,  $S_i$  is the area  
257 covered by the conditioning factor and  $S$  is the total area of the study region.

### 258 **3.1.3 Buffer distance optimization and uncertainty assessment for LSP**

259 To generate negative (non-landslide) samples for LSP, areas within buffer distances of  $d$   
260 = 0.1, 0.5, 1.0, 2.0, and 5.0 km around landslide locations were excluded, with balanced  
261 negative samples ( $n = 705$ ) randomly selected from remaining stable areas for each distance.  
262 The optimal buffer distance was determined by evaluating SVM and LightGBM model  
263 performance using AUC, Precision, Recall, and F1-score metrics.

264 The selection of buffer distances (0.1–5.0 km) was based on Zixing's geomorphological  
265 considerations and practices commonly reported in LSP. This range encompasses multiple  
266 spatial scales: slope-scale processes (0.1–0.5 km), catchment-scale features (1.0–2.0 km), and  
267 regional-scale geological units (5.0 km). The evaluation ensures optimal spatial representation  
268 without a priori assumptions about scale dependencies (Chang et al., 2023).

269 Prediction uncertainty was assessed using the mean and standard deviation (SD) of  
270 predicted landslide susceptibility values. Lower mean and SD values indicate reduced  
271 prediction uncertainty and more concentrated susceptibility patterns, suggesting higher model  
272 confidence in LSP (Huang et al., 2022), thereby complementing the buffer distance  
273 optimization process.

## 274 **3.2 Effective rainfall threshold modeling**

### 275 **3.2.1 Rainfall parameterization and threshold calculation**

276 Typhoon-induced landslides are generally influenced by a combination of antecedent  
277 moisture conditions and immediate precipitation, rather than by isolated rainfall events  
278 (Mondini et al., 2023; Tufano et al., 2021). To account for the cumulative impact of multi-day

279 rainfall while incorporating hydrological processes such as evapotranspiration and drainage,  
280 we adopted the concept of effective rainfall ( $P_e$ ), calculated as:

281

$$P_e = \sum_{i=0}^n k^i P_i \quad (7)$$

282 where  $P_i$  represents the daily rainfall on the  $i$ -th day preceding landslide occurrence,  $n$  denotes  
283 the number of antecedent days considered, and  $k$  is the effective rainfall decay coefficient  
284 (Segoni et al., 2018a). For hourly rainfall parameterization,  $P_i$  is derived as:

285

$$P_i = \sum_{j=1}^{24} R_{ij} \quad (8)$$

286 where  $R_{ij}$  is the hourly rainfall at the  $j$ -th hour of the  $i$ -th day.

287 **3.2.2 Long-term and short-term rainfall parameters**

288 Rainfall-triggered landslides are generally triggered by two dominant mechanisms:  
289 prolonged low-intensity rainfall and short-duration high-intensity storms. Based on statistical  
290 analysis of historical landslide events in Hunan Province (Xiao et al., 2025), a 7-day  
291 antecedent period was identified as optimal for characterizing long-term rainfall impacts.  
292 Consequently, the 7-day effective rainfall (D7) was selected as the long-term parameter.  
293 Short-term rainfall metrics were defined as cumulative precipitation over 1 hour (H1), 12  
294 hours (H12), 24 hours (H24), and 72 hours (H72) preceding landslide initiation. These  
295 intervals capture distinct rainfall characteristics: H1 reflects extreme short-term intensity for  
296 rapid slope failures, H12 and H24 represent sub-daily to daily precipitation critical for  
297 intermediate responses, and H72 accounts for multi-day storm sequences.

298 **3.2.3 Rainfall threshold model development**

299 The threshold modeling framework comprises four sequential steps:

300 (1) Parameter calculation: The threshold modeling framework comprises four sequential  
301 steps: (1) Parameter calculation: For each landslide sample, short-term rainfall parameters (H1,  
302 H12, H24, and H72) and the long-term rainfall parameter (D7) are calculated. The ratios of

303 short-term parameters to the long-term parameter are computed as:  $R1=H1/D7$ ,  $R12=H12/D7$ ,  
304  $R24=H24/D7$ , and  $R72=H72/D7$ .

305 (2) Threshold setting: Long-to-short-term ratio coefficients ( $RC1$ ,  $RC12$ ,  $RC24$ , and  
306  $RC72$ ) are introduced as thresholds to determine the dominant rainfall pattern for each  
307 landslide. These thresholds are used to classify landslides into short-term or long-term  
308 Typhoon-induced categories.

309 (3) Coefficient optimization: A cyclic trial-and-error method is employed to determine  
310 the optimal ratio coefficients ( $RC1$ ,  $RC12$ ,  $RC24$ , and  $RC72$ ), maximizing the accuracy and  
311 reliability of the model.

### 312 **3.2.4 Optimal ratio coefficient threshold determination**

313 The process of determining the optimal long-to-short-term ratio coefficient threshold is  
314 demonstrated using  $H12-D7$  as an example. The process for the remaining coefficients ( $H1-D7$ ,  
315  $H24-D7$ , and  $H72-D7$ ) follows a similar approach. A 5-fold cross-validation method is  
316 applied, with the following procedure:

317 (1) Rainfall data extraction for landslide locations: For each of the 705 landslide points,  
318  $R12$  and  $D7$  values are extracted from these interpolated surfaces at the exact landslide  
319 coordinates, ensuring that each landslide location receives rainfall values derived from the  
320 spatially weighted contributions of all nearby gauge stations.  $R12$  and  $D7$  values for each  
321 landslide are calculated using Equations (7) and (8).

322 (2) Data preparation: The dataset is divided into five equal parts for cross-validation,  
323 with each part serving as a test set while the remaining four serve as the training set.

324 (3) Initial threshold setting: An initial threshold for  $RC12$  is set based on the minimum  
325 value in the training set.

326 (4) Threshold evaluation: For each fold, the  $RC12$  threshold is compared with the  $R12$   
327 value of samples in the test set. If  $RC12 < R12$ , the prediction is considered a failure.

328 Prediction accuracy is calculated for each RC12 threshold, adjusting in 0.001 increments until  
329 the highest prediction accuracy is achieved.

330 (5) Optimal RC12 threshold determination: The RC12 threshold with the highest  
331 prediction accuracy is selected for each fold. The final RC12 threshold is determined by  
332 averaging the optimal thresholds from all five folds.

### 333 **3.2.5 Spatial distribution of optimal threshold**

334 According to the optimal ratio coefficient threshold determined in section 3.2.4 and the  
335 long-term and short-term rainfall parameters obtained through interpolation, the threshold  
336 spatial distribution for the study area can be derived. Taking H12/D7 as an example, the  
337 process is as follows:

338 First, by dividing the H12 values of each landslide point by the optimal ratio coefficient  
339 RC12, the corresponding D7 thresholds for each landslide point can be calculated. These D7  
340 thresholds serve as a basis for applying the Kriging interpolation method to obtain the spatial  
341 distribution map of the D7 thresholds across the entire study area.

342 Next, by multiplying the D7 values of each landslide point by the ratio coefficient RC12,  
343 the corresponding H12 thresholds for each landslide point can be determined. Subsequently,  
344 utilizing these H12 thresholds, the Kriging interpolation method is applied once more to  
345 generate the spatial distribution map of the H12 thresholds for the entire study area.

## 346 **3.3 Typhoon-specific rainfall-induced landslide warning system**

347 In order to effectively prevent typhoon-specific rainfall-induced landslide hazards,  
348 constructing a comprehensive landslide warning system is crucial. This system integrates LSP  
349 with critical rainfall thresholds, combining spatial probability and temporal probability to  
350 predict the risk of landslide occurrence and the timing of potential events.

### 351 **3.3.1 Construction of the landslide warning system**

352 Using the natural breaks point method, the LSP is categorized into five levels of spatial  
 353 probability: very low (S1), low (S2), moderate (S3), high (S4), and very high (S5). These  
 354 levels represent varying degrees of susceptibility to landslides in different regions, forming  
 355 the basis for assessing landslide risks when combined with rainfall data. Paralleling the LSP  
 356 categorization, rainfall thresholds are also divided into five levels using the natural breaks  
 357 point method, representing temporal probability: very low (T1), low (T2), moderate (T3),  
 358 high (T4), and very high (T5). A lower rainfall threshold indicates a higher likelihood of  
 359 typhoon-induced landslides, thus signaling a greater risk of landslide events.

360 **Table 2** Classification of landslide hazard warning zones by integrating landslide susceptibility levels  
 361 (S1~S5) with rainfall threshold levels (T1~T5).

Landslide hazard warning zones	T1	T2	T3	T4	T5
S1 (very low)	No warning zone (2 <sup>nd</sup> level)	No warning zone (1 <sup>st</sup> level)			
S2 (low)	3 <sup>rd</sup> level warning zone	No warning zone (2 <sup>nd</sup> level)	No warning zone (2 <sup>nd</sup> level)	No warning zone (1 <sup>st</sup> level)	No warning zone (1 <sup>st</sup> level)
S3 (moderate)	4 <sup>th</sup> level warning zone	3 <sup>rd</sup> level warning zone	3 <sup>rd</sup> level warning zone	No warning zone (2 <sup>nd</sup> level)	No warning zone (1 <sup>st</sup> level)
S4 (high)	5 <sup>th</sup> level warning zone	4 <sup>th</sup> level warning zone	3 <sup>rd</sup> level warning zone	No warning zone (2 <sup>nd</sup> level)	No warning zone (1 <sup>st</sup> level)
S5 (very high)	5 <sup>th</sup> level warning zone	5 <sup>th</sup> level warning zone	4 <sup>th</sup> level warning zone	3 <sup>rd</sup> level warning zone	No warning zone (2 <sup>nd</sup> level)

362 The matrix-based integration of LSP results and rainfall thresholds, as presented in Table  
 363 2 (Segoni et al., 2015), highlight the correlation between landslide susceptibility and rainfall  
 364 intensity. As the levels of landslide hazard warnings escalate from the 1<sup>st</sup> level, indicating no  
 365 warning, to the 5<sup>th</sup> level, which signifies the highest alert, the likelihood of landslide  
 366 occurrences correspondingly increases. Areas categorized in higher hazard zones correspond  
 367 to regions with a heightened risk of landslides. **This hazard warning system provides a spatial  
 368 framework for risk assessment and early warning, generating hazard zonation maps that can  
 369 be integrated into operational landslide monitoring and warning protocols.** This underscores  
 370 the importance of implementing more effective geological disaster prevention strategies, as  
 371 thoroughly discussed in the literature by Huang et al. (2022).

372 **4.Landslide susceptibility prediction using machine learning models**

373 **4.1 Statistical analysis of conditioning factors**

374 The statistical analysis reveals distinct patterns of landslide susceptibility across all  
375 conditioning factors (Table S1 in the Supplement). Topographic factors demonstrate clear  
376 elevation-dependent behavior, with maximum susceptibility occurring at intermediate  
377 elevations (545-782 m, FR=1.637, IV=0.389), suggesting optimal conditions where  
378 weathering processes and slope instability converge. Slope gradient exhibits peak  
379 susceptibility in the moderate range (7.87-15.06°, FR=1.522, IV=0.343), indicating  
380 insufficient driving forces at gentler slopes and potential debris removal at steeper gradients.  
381 South-facing aspects show enhanced susceptibility (FR=1.299, IV=0.230), likely attributable  
382 to intensified weathering from solar radiation and moisture cycles.

383 Morphological indices reveal significant correlations with landslide occurrence. Profile  
384 curvature demonstrates highest susceptibility in convex areas (0.17-0.59, FR=1.480,  
385 IV=0.480), where stress concentration promotes slope failure. TWI shows strong positive  
386 correlation with wetness, peaking at high values (8.69-13.62, FR=1.799, IV=0.444),  
387 confirming the critical role of water accumulation in slope destabilization. SPI indicates  
388 maximum susceptibility in moderate stream power ranges (1.27-2.39, FR=1.298, IV=0.229),  
389 reflecting optimal erosional conditions.

390 Proximity factors exhibit contrasting patterns based on infrastructure type. Distance to  
391 roads shows strong inverse correlation with landslide occurrence (0-800 m, FR=1.499,  
392 IV=0.333), indicating anthropogenic disturbance effects. Conversely, distance to faults  
393 reveals a bimodal pattern with peak susceptibility at intermediate distances (7-12 km,  
394 FR=1.439, IV=0.305), suggesting regional structural influence rather than localized fault-  
395 induced instability. Environmental factors demonstrate vegetation's protective role, with  
396 moderate NDVI values (0.64-0.76) showing elevated susceptibility (FR=1.854, IV=0.015),

397 representing the transition zone between bare soil vulnerability and established vegetation  
398 stability. Lithological analysis reveals pronounced material control, with rhyolite (FR=1.546,  
399 IV=0.353) and granite (FR=1.247, IV=0.198) showing enhanced susceptibility due to  
400 intensive weathering and joint development, while sedimentary rocks (slate, shale, limestone,  
401 sandstone) exhibit strong resistance (FR<0.21) owing to their structural integrity and lower  
402 weathering susceptibility.

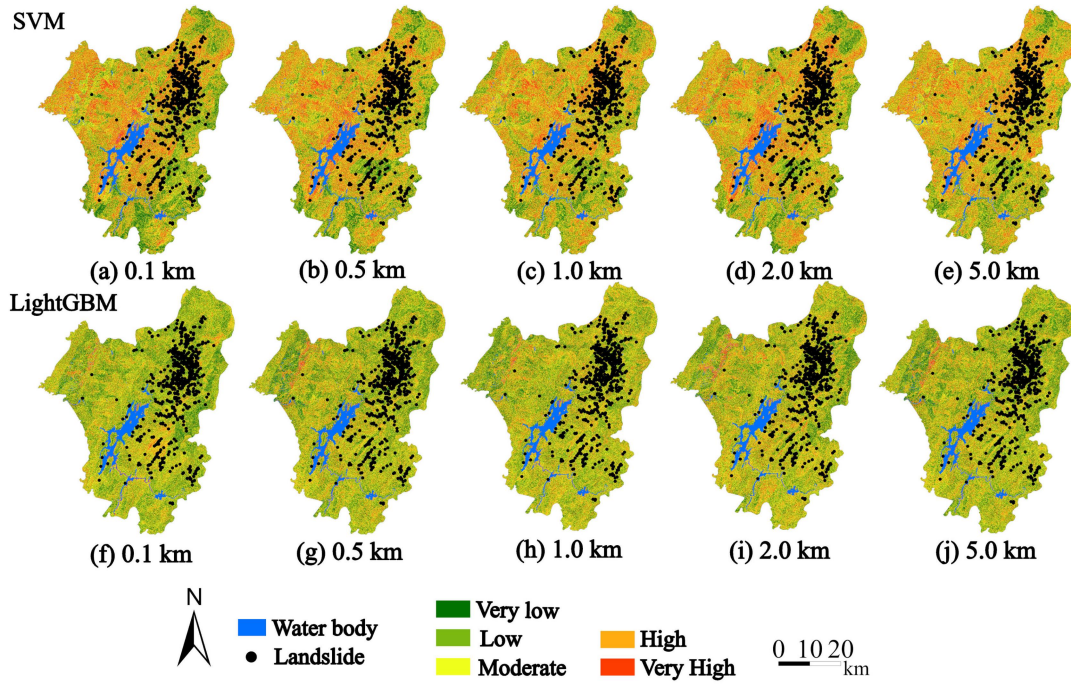
## 403       **4.2 Landslide susceptibility modeling in Zixing City**

404       Prior to model development, multicollinearity analysis was conducted using variance  
405 inflation factor (VIF) to ensure statistical reliability of the conditioning factors. The analysis  
406 revealed method-specific multicollinearity patterns: IV and CF methods showed no  
407 significant multicollinearity issues (all VIF < 10), while the FR method exhibited  
408 multicollinearity in four variables (SPI, Aspect, Plan curvature, and Distance to rivers with  
409 VIF > 10), which were subsequently excluded from FR-based modeling (Table S2 in the  
410 supplement). Following this preprocessing, landslide susceptibility prediction was performed  
411 using SVM and LightGBM models with the three distinct weighting methods (IV, CF, and  
412 FR). Susceptibility levels were categorized into five classes using the natural breaks  
413 classification method, with non-landslide samples strategically selected by excluding buffer  
414 zones of varying distances (0.1, 0.5, 1.0, 2.0, and 5.0 km) around documented landslide  
415 locations to optimize model performance and reduce spatial bias.

### 416       **4.2.1 IV-based modeling performance**

417       The IV-derived susceptibility maps (Fig. 4) revealed distinct spatial patterns between the  
418 two models across varying buffer distances. At smaller scales, the SVM model demonstrated  
419 more detailed classification, with a higher degree of overlap between high susceptibility areas  
420 and actual landslide locations. The LightGBM model's classification was smoother, with a  
421 lower degree of overlap between high susceptibility areas and actual landslide locations.

422 Notably, this performance discrepancy diminished progressively with increasing buffer  
423 distances.



424

425 **Figure 4** Landslide susceptibility map based on SVM and LightGBM models using the IV input.

#### 426 **4.2.2 CF-based modeling performance**

427 In CF-based modeling (Fig. 5), the SVM model's high and very high landslide  
428 susceptibility areas at smaller scales were more extensive than in the IV mode, with actual  
429 landslide locations more frequently distributed within these high-risk areas. As the scale  
430 increased, the high susceptibility areas gradually decreased. The LightGBM model also  
431 showed a relatively smooth distribution, with some high susceptibility areas identified at  
432 smaller scales gradually integrating as the scale increased, following a similar trend to the  
433 SVM model.

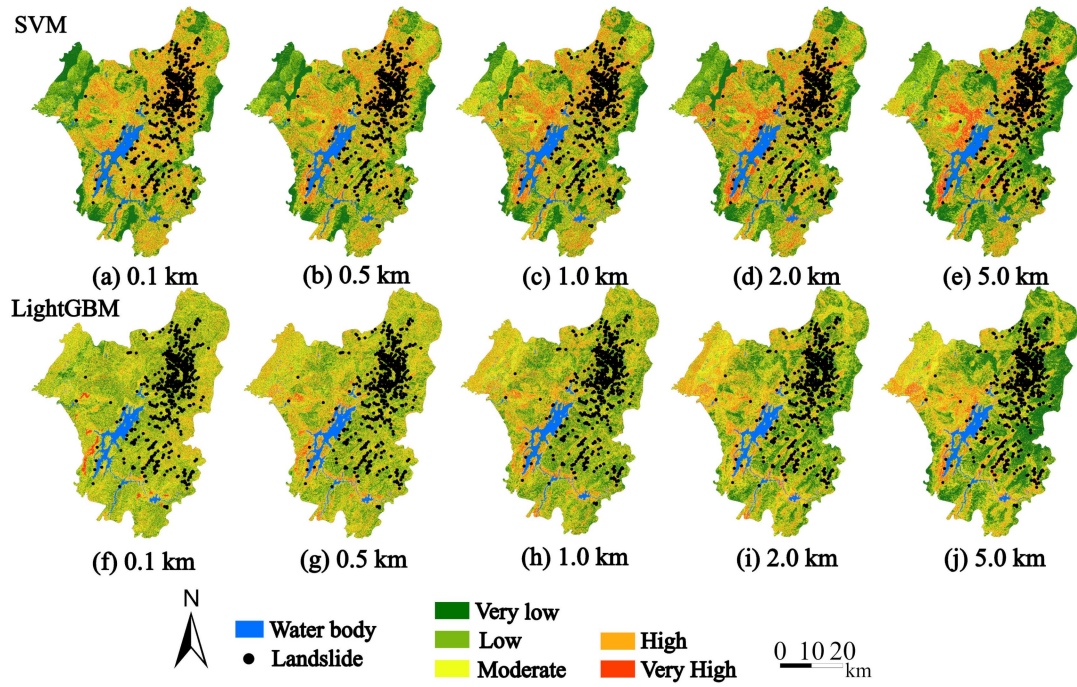


**Figure 5** Landslide susceptibility map based on SVM and LightGBM models using the CF input.

#### 4.2.3 FR-based modeling performance

437 Regarding the FR input (Fig. 6), the SVM model identified a significant number of high  
 438 and very high landslide susceptibility areas at smaller scales compared to the IV and CF  
 439 inputs, which closely matched the actual locations of landslides. As the buffer scale expanded,  
 440 these high-risk areas generally diminished and the distribution became smoother. Conversely,  
 441 the LightGBM model delivered more uniform results, offering broader moderate-risk  
 442 distributions, with a small number of high susceptibility areas that did not align with the  
 443 actual landslide locations. As the scale increased, the high susceptibility areas identified by  
 444 the LightGBM model gradually diminished, showing greater consistency with the SVM  
 445 model results at the higher scale.

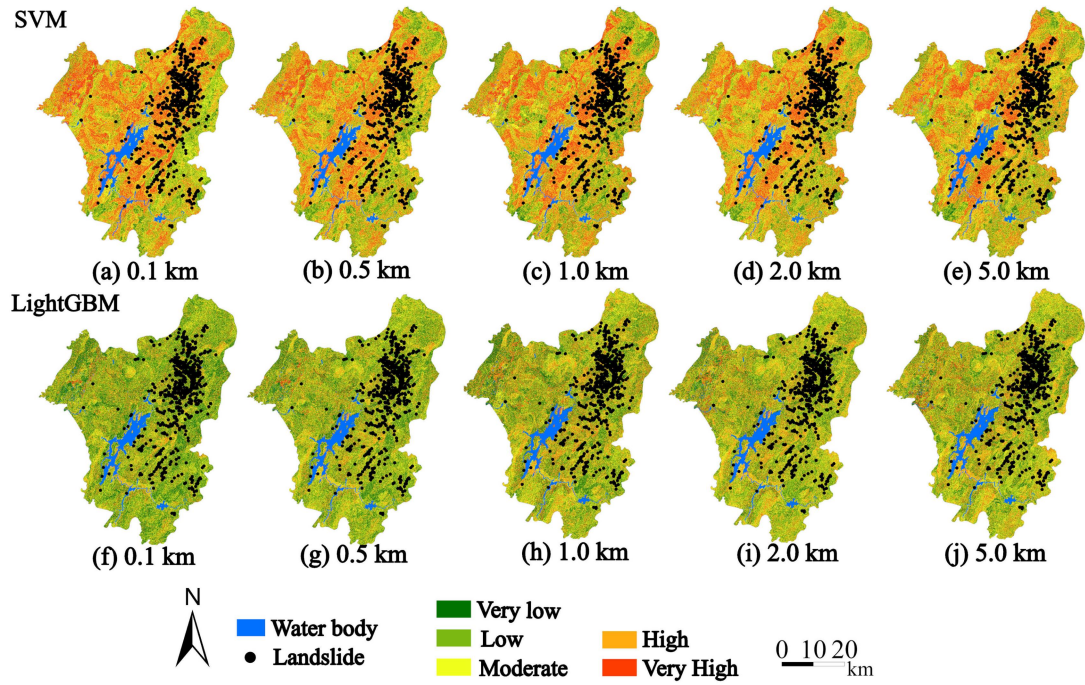


Figure 6 Landslide susceptibility map based on SVM and LightGBM models using the FR input.

### 4.3 Uncertainty analysis of LSP results

#### 4.3.1 LSP accuracy evaluation and comparative performance

Table S2 (in the Supplement) demonstrates contrasting performance characteristics between the two machine learning approaches across different spatial scales and input configurations. LightGBM consistently achieved high AUC values (0.915-0.921) and maintained stable F1-scores (0.838-0.850) across all buffer distances and input methods, indicating robust generalization capability. In contrast, SVM exhibited pronounced sensitivity to parameter combinations, with performance varying significantly across different buffer distances (F1-scores ranging from 0.681 to 0.859) and input methods, particularly showing notable degradation with FR input at extreme spatial scales (0.1 km and 5.0 km).

Two configurations emerged as comprehensively superior: SVM with FR input at 0.5 km and 2.0 km buffer distances, both achieving F1-scores of 0.859. These optimal configurations not only maintained competitive AUC values (0.914 and 0.913 respectively) but demonstrated superior precision-recall balance compared to corresponding LightGBM configurations (F1-scores: 0.854 and 0.856). The high recall values (0.845 and 0.851) coupled with robust

463 precision (0.873 and 0.867) indicate enhanced sensitivity to landslide-prone areas while  
464 minimizing false positive predictions. This bimodal performance pattern suggests that  
465 intermediate buffer distances effectively capture fault-related geomorphological processes  
466 influencing slope stability.

467 Independent validation on the test set confirmed the robustness of these optimal  
468 configurations, with SVM-FR models at 0.5 km and 2.0 km buffer distances achieving F1-  
469 scores of 0.847 and 0.852 respectively, representing minimal performance degradation from  
470 training results. The consistent AUC values (0.909 and 0.908) on the test set further validate  
471 the models' discriminative capability and indicate absence of overfitting, confirming the  
472 reliability of these configurations for practical landslide susceptibility assessment applications.

473 **4.3.2 LSP distribution characteristics across conditions**

474 In addition to the performance metrics, the distribution characteristics of landslide  
475 susceptibility predictions revealed fundamental differences between the models (Figs. S1–S3  
476 in the Supplement). LightGBM generated smoother, more symmetrical distributions with  
477 lower mean susceptibility values (0.196–0.320) and smaller standard deviations (0.099–  
478 0.187), indicating stable and uniform predictions. In contrast, SVM exhibited greater  
479 variability, with irregular distributions, higher mean values (0.303–0.515), and larger standard  
480 deviations (0.112–0.214). Notably, SVM's mean susceptibility under FR input rose sharply  
481 (0.446–0.515), while LightGBM maintained lower means despite moderately broader  
482 deviations (0.160–0.187).

483 Therefore, SVM is preferable for FR-based modeling at 0.5 km and 2.0 km buffers,  
484 where spatial precision is prioritized over prediction uniformity. The SVM model achieved its  
485 highest accuracy at the 0.5 km buffer, classifying 86.4% of recorded landslides in high and  
486 very high susceptibility zones (Fig. 6 (b)). At the 2.0 km buffer (Fig. 6 (d)), it still correctly

487 classified 82.1% of landslides in these zones. As a result, Fig. 6 (b) is selected as the final  
488 landslide susceptibility map.

489 **5 Landslide risk assessment in Zixing City**

490 **5.1 Critical rainfall thresholds for landslides in Zixing City**

491 We evaluated four rainfall threshold models (H1-D7, H12-D7, H24-D7, and H72-D7)  
492 through 5-fold cross-validation, with their optimal ratio coefficient (RC) thresholds and  
493 prediction accuracies summarized in Table 3. The H24-D7 model, coupling 24-hour rainfall  
494 during landfall with 7-day antecedent moisture, achieved the highest accuracy (71.8%) by  
495 effectively capturing both cumulative saturation and abrupt triggering by typhoon rainfall  
496 bursts. Notably, the H24-D7 model exhibited stable performance across all folds, with  
497 accuracy ranging narrowly between 68.8% (Fold 1) and 74.6% (Fold 4), reflecting robust  
498 generalizability.

499 **Table 3** Optimal RC values and prediction accuracies (%) for each model across 5-fold cross validation.

Model	Fold 1 RC/Accuracy	Fold 2 RC/Accuracy	Fold 3 RC/Accuracy	Fold 4 RC/Accuracy	Fold 5 RC/Accuracy	Average RC/Accuracy
H1-D7	0.032/56.5	0.062/29.7	0.076/35.5	0.022/53.6	0.040/47.8	0.047/44.6
H12-D7	0.077/54.2	0.167/46.6	0.243/48.3	0.267/47.7	0.154/45.3	0.182/48.5
H24-D7	0.472/68.8	0.436/72.3	0.422/73.1	0.459/74.6	0.414/70.2	<b>0.440/71.8</b>
H72-D7	0.789/56.5	0.776/59.4	0.781/63.1	0.802/51.4	0.783/60.1	0.787/58.1

500 In contrast, the H1-D7 and H12-D7 models displayed marked instability: H1-D7  
501 accuracy fluctuated between 29.7% (Fold 2) and 56.5% (Fold 1), while H12-D7 thresholds  
502 (RC12: 0.077–0.267) corresponded to accuracies of 45.3–48.3%. The H72-D7 model showed  
503 moderate performance variability (accuracy: 51.4–63.1%) despite consistently high RC72  
504 thresholds (>0.78).

505 These results highlight the critical role of temporal rainfall parameter selection. The  
506 superior performance of the H24-D7 model (24-hour short-term rainfall and 7-day antecedent  
507 rainfall) suggests that a 24-hour duration optimally captures both immediate landslide triggers

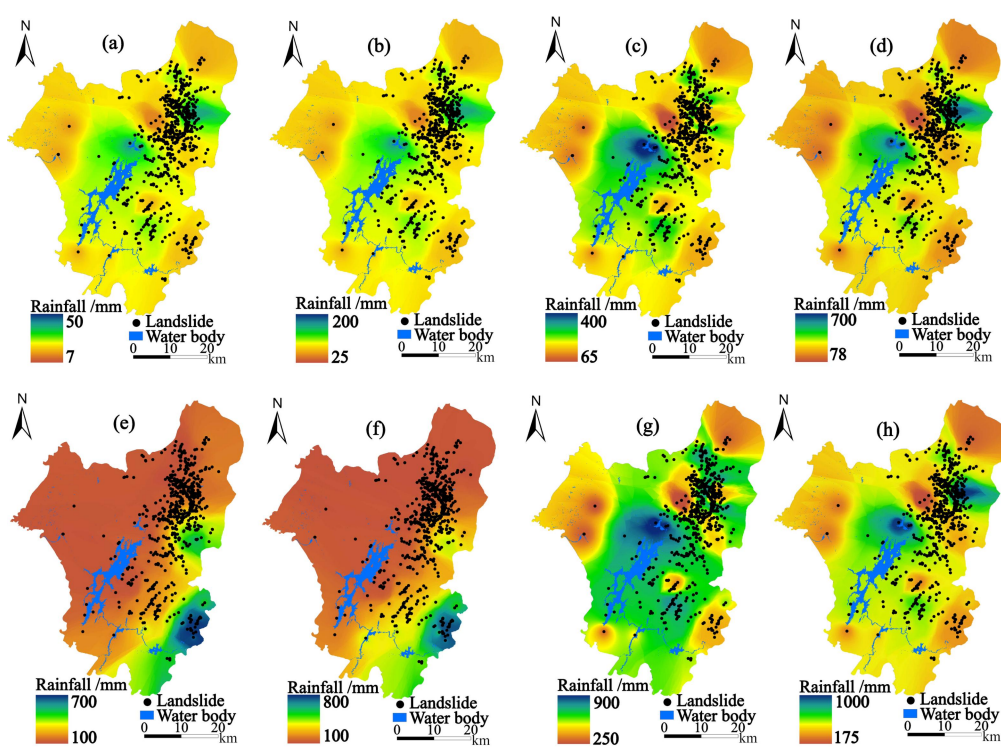
508 and cumulative hydrological effects, balancing sensitivity and stability. Shorter (H1/H12) or  
509 longer (H72) durations either overemphasize transient rainfall spikes or dilute critical  
510 triggering signals.

## 511 5.2 Spatio-temporal distribution of rainfall thresholds

512 Fig. 7 illustrates the spatial distribution of rainfall-triggered landslide thresholds derived  
513 from four models (RC1, RC12, RC24, and RC72) across multiple temporal scales (1-hour,  
514 12-hour, 24-hour, 72-hour, and 7-day) within the study area.

### 515 5.2.1 Short-term predictions (1-hour to 12-hour scales)

516 At the 1-hour scale (Fig. 7 (a)), the RC1 model generated thresholds ranging from 7 to  
517 50 mm, with 65.2% of landslides occurring in moderate threshold zones (20-30 mm). This  
518 indicates the model's effectiveness in detecting slope failures under short-duration rainfall. In  
519 contrast, the RC12 model on the 12-hour scale (Fig. 7 (b)) showed a wider threshold range  
520 (25-200 mm), with 62.9% of landslides in mid-to-high threshold regions (80-130 mm). This  
521 mismatch suggests that the 12-hour cumulative data may underestimate rainfall impacts in  
522 specific topographic settings.



523

524      **Figure 7** Distribution of typhoon rainfall thresholds under various optimal RC ratios: (a) 1-hour RC1-based, (b)  
525      12-hour RC12-based, (c) 24-hour RC24-based, (d) 72-hour RC72-based, (e) 7-day RC1-based, (f) 7-day RC12-  
526      based, (g) 7-day RC24-based, and (h) 7-day RC72-based.

527      **5.2.2 Mid-term predictions (24-hour to 72-hour scales)**

528      The RC24 model at the 24-hour scale (Fig. 7 (c)) displayed a threshold range of 65-400  
529      mm, with 87.1% of landslides occurring within moderate thresholds (100-250 mm) and  
530      12.3% in higher thresholds (>250 mm). This indicates a more accurate capture of rainfall  
531      intensity effects. At the 72-hour scale (Fig. 7 (d)), the RC72 model produced thresholds  
532      between 78-700 mm, with 59.2% of landslides in mid-to-high threshold regions (200-500  
533      mm). Although the RC72 model demonstrated reasonable sensitivity to prolonged rainfall, its  
534      upper threshold (700 mm) may result in conservative risk predictions for some geological  
535      settings.

536      **5.2.3 Long-term predictions (7-day scale)**

537      At the 7-day scale, significant differences emerge across models in terms of predicted  
538      rainfall thresholds and landslide points. The RC1 model (Fig. 7 (e)) shows a threshold range  
539      of 100-700 mm, with landslide points predominantly concentrated in the lower rainfall ranges.  
540      While these low-threshold landslides may indicate localized risks, the model's conservative  
541      threshold distribution fails to effectively capture landslides triggered by higher rainfall  
542      amounts, potentially overlooking more significant events.

543      The RC12 model (Fig. 7 (f)), with a threshold range of 100-800 mm, also shows a  
544      concentration of landslide points in the lower rainfall ranges. Despite a wider threshold range,  
545      the similarity to the RC1 model suggests that RC12 may also underutilize its capacity to  
546      predict higher typhoon-induced landslides, leading to under-prediction in areas experiencing  
547      moderate to heavy precipitation.

548      In contrast, the RC24 model (Fig. 7 (g)) exhibits a balanced threshold range (250-900  
549      mm) and effectively identifies landslide points in both moderate and high rainfall categories.

550 This balance enables RC24 to capture the full spectrum of typhoon-induced landslides,  
551 accurately identifying risks across different rainfall intensities.

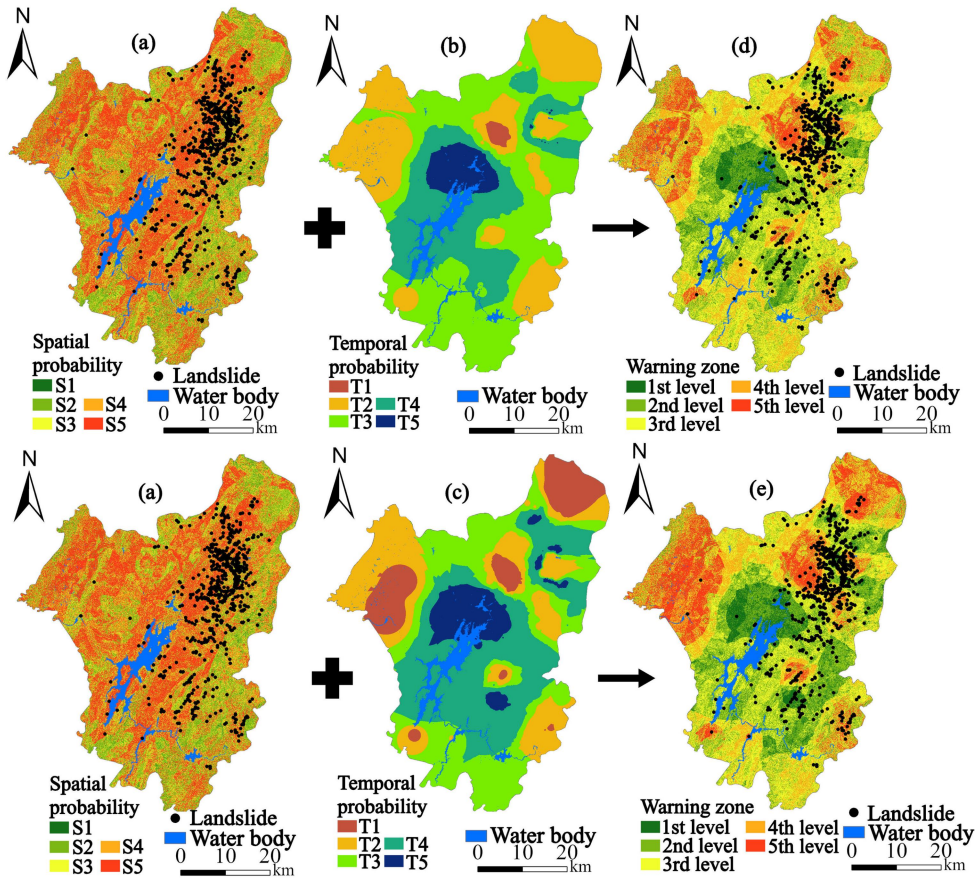
552 The RC72 model (Fig. 7 (h)) shows a concentration of landslide points in the higher  
553 rainfall range (175-1000 mm). While it predicts landslides accurately under heavy rainfall  
554 conditions, the model may overestimate risks in some regions and neglect potential landslides  
555 associated with lower rainfall thresholds.

556 Based on the above analysis, the RC24 model is the optimal choice, which aligns with  
557 the finding in Section 5.1. Its effectiveness is evident as it demonstrates superior stability and  
558 accuracy in both the 24-hour and 7-day timescales. The RC24 model's balanced threshold  
559 range allows it to accurately assess landslide risks across varying rainfall intensities. This  
560 makes it the most reliable choice for practical landslide hazard warning applications.

561 **5.3 Landslide hazard warning system for Zixing City**

562 Based on the optimal LSP results (Fig. 6 (b)) and the validated RC24 rainfall threshold  
563 model, a spatially explicit landslide hazard warning system was established for Zixing City.  
564 The integration of spatial probability (LSP) and temporal probability (rainfall thresholds)  
565 followed the matrix classification outlined in Table 2.

566



567 **Figure 8** Landslide warning zones generated by overlaying spatial and temporal probability maps: (a) optimal  
 568 spatial probability, (b) 24-hour RC24-based rainfall threshold, (c) 7-day RC24-based rainfall threshold, (d)  
 569  
 570 overlay of (a) and (b), and (e) overlay of (a) and (c).

571 Five susceptibility levels in the LSP map (Fig. 6 (b)) were replaced with five spatial  
 572 probabilities (S1–S5) (Fig. 8 (a)), respectively. Simultaneously, the spatially interpolated 24-  
 573 hour rainfall thresholds (H24) (Fig. 8 (b)) and 7-day effective rainfall thresholds (D7) (Fig. 8  
 574 (c)) derived from the RC24 model were classified into five temporal probability levels (T1–  
 575 T5) using the natural breaks method. Spatial overlay analysis was performed to combine the  
 576 susceptibility levels (S1–S5) with the rainfall threshold levels (T1–T5), generating two hazard  
 577 warning zone maps: H24-based (Fig. 8 (d)) and D7-based (Fig. 8 (e)).

578 Quantitative assessment of both warning systems reveals distinct performance  
 579 characteristics. The 24-hour threshold system (Fig. 8 (d)) demonstrates superior predictive  
 580 efficiency, with 71.4% of historical landslides occurring within high to very high warning  
 581 zones (Levels 3–5) while covering only 34.2% of the total area, resulting in an efficiency ratio

582 of 2.09 and a risk density of 49.0 landslides per 1000 high-risk grid cells. The spatial  
583 distribution shows concentrated high-risk areas primarily in the central region, characterized  
584 by steep slopes ( $>21.80^\circ$ ), weathered granite lithology, and road proximity (0–800 m). This  
585 focused distribution indicates effective identification of areas most sensitive to short-term  
586 intense rainfall triggers.

587 The 7-day threshold system (Fig. 8 (e)) exhibits broader spatial coverage, with high-risk  
588 zones encompassing 42.7% of the study area and capturing 68.7% of historical landslides,  
589 yielding a lower efficiency ratio of 1.61 and risk density of 37.8 landslides per 1000 grid cells.  
590 This system effectively identifies extended vulnerable areas in northern and eastern regions,  
591 reflecting cumulative rainfall effects on slope stability. The expanded coverage captures zones  
592 where prolonged antecedent moisture interacts with moderate-to-high susceptibility  
593 conditions.

594 Statistical validation confirms the complementary nature of both systems. The 24-hour  
595 system achieves higher spatial efficiency (efficiency ratio 2.09 vs. 1.61) and landslide  
596 concentration (risk density 49.0 vs. 37.8), making it optimal for immediate typhoon response  
597 and targeted emergency resource allocation. Conversely, the 7-day system provides  
598 comprehensive coverage for prolonged rainfall scenarios, essential for early warning during  
599 extended typhoon events despite its broader spatial distribution and lower concentration  
600 efficiency. The combined application of both systems enables dynamic hazard assessment,  
601 addressing both rapid-onset failures during typhoon landfall and delayed failures following  
602 sustained precipitation.

603 **6 Discussion**

604 **6.1 Optimization of landslide susceptibility prediction**

605 Our comparative analysis of SVM and LightGBM models across different input methods  
606 (IV, CF, FR) and buffer distances revealed important insights into the optimization of LSP

607 under typhoon-specific rainfall conditions. SVM's superior performance at buffer distances of  
608 0.5–2.0 km with FR inputs highlights the importance of spatial scale selection in typhoon-  
609 induced landslide modeling. This extends existing research (Kalantar et al., 2018; Bogaard  
610 and Greco, 2018) by identifying typhoon-specific spatial patterns that diverge from  
611 conventional rainfall scenarios.

612 The optimal 0.5–2.0 km buffer range corresponds to the spatial autocorrelation pattern of  
613 typhoon-induced failures, where intense moisture infiltration generates discrete instability  
614 zones. This differs markedly from earthquake-triggered landslides, which cluster at finer  
615 scales (Fan et al., 2019), reflecting typhoons' distinct hydrological impact. The effectiveness  
616 of FR weighting is consistent with the findings of Reichenbach et al. (2018) and Yan et al.  
617 (2019), who demonstrated that frequency-based methods effectively capture non-linear  
618 relationships between factors in complex terrain. Our findings indicate FR's particular  
619 strength under typhoon conditions stems from its capacity to capture specific factor  
620 interactions, including how road networks intensify runoff concentration on weathered granite  
621 slopes (Liu et al., 2022).

## 622 **6.2 Rainfall threshold modeling and typhoon-specific mechanisms**

623 The H24-D7 model's superior performance (71.8% accuracy) marks a significant  
624 advancement in understanding the triggering mechanisms of typhoon-specific landslides. This  
625 temporal window effectively captures the dual-phase nature of typhoon-induced slope failure:  
626 prolonged antecedent saturation from tropical moisture bands followed by critical threshold  
627 exceedance during typhoon core passage (Kirschbaum and Stanley, 2018). The model's  
628 effectiveness validates the conceptual framework proposed by Nolasco-Javier and Kumar  
629 (2018), who emphasized the importance of multi-temporal rainfall accumulation in tropical  
630 cyclone environments.

631 The spatial heterogeneity in rainfall thresholds reflects the complex interaction between  
632 typhoon structure and local topography (Lee et al., 2018; Cho et al., 2022). Higher thresholds  
633 in southeastern slopes (>250 mm) correspond to areas of enhanced orographic lifting (Fig.  
634 7(c)), where terrain amplifies typhoon rainfall through forced ascent mechanisms. Conversely,  
635 lower thresholds in northern valleys (100-150 mm) (Fig. 7(c)) indicate areas where  
636 topographic channeling and moisture convergence create favorable conditions for slope  
637 failure at reduced precipitation levels. This spatial variability contradicts the assumption of  
638 uniform regional thresholds commonly applied in operational warning systems (Segoni et al.,  
639 2018b) and supports the implementation of spatially distributed threshold approaches.

640 The H24-D7 model's robust cross-validation performance (68.8-74.6% across folds)  
641 demonstrates its stability across different typhoon sub-events and rainfall patterns. This  
642 consistency is crucial for operational implementation, as typhoons exhibit significant internal  
643 variability in rainfall distribution and intensity (Liu et al., 2017). The model's ability to  
644 maintain predictive accuracy across this variability represents a substantial improvement over  
645 traditional empirical threshold approaches that often fail during extreme events (Guzzetti et al.,  
646 2020).

### 647 **6.3 Integration of susceptibility and rainfall thresholds for landslide warning**

648 Integrating landslide susceptibility and rainfall thresholds in an early warning system  
649 creates a dynamic framework for real-time monitoring and assessment of landslide hazards.  
650 By overlaying static susceptibility maps with real-time precipitation data, this approach offers  
651 a continuous hazard assessment that adapts to changing weather conditions, particularly  
652 during typhoons. The system updates hazard assessments hourly, reflecting the evolving  
653 precipitation patterns that drive landslide potential.

654 The operational framework consists of three hierarchical components: (1) static  
655 susceptibility surfaces derived from optimized Support Vector Machine-based Flood Risk

656 (SVM-FR) models, which act as baseline hazard zones, (2) dynamic threshold surfaces (H24  
657 and D7) that define conditions under which rainfall triggers landslide activation, and (3) real-  
658 time precipitation monitoring, which drives continuous hazard updates. These components  
659 work together to ensure a comprehensive and up-to-date hazard assessment.

660 One of the key features of this system is its ability to automatically adjust warning levels  
661 based on meteorological forecasts. When forecasts indicate a greater than 70% probability of  
662 threshold exceedance in high-susceptibility areas, the system escalates warning levels  
663 accordingly, providing timely alerts to mitigate disaster risk (Piciullo et al., 2018). The dual-  
664 threshold configuration enhances this approach by providing temporal staging suited to the  
665 dynamic nature of typhoons. Specifically, as a typhoon approaches (48-72 hours before  
666 landfall), the D7 threshold monitors antecedent rainfall to identify areas nearing saturation  
667 and instability. As the typhoon intensifies and makes landfall, the H24 threshold responds to  
668 immediate, intensive rainfall events, triggering warnings for zones that experience rapid  
669 threshold exceedance (Gariano et al., 2015). This staged warning system ensures optimized  
670 lead times for alerts, while also minimizing the risk of alert fatigue, a common challenge in  
671 continuous hazard monitoring (Nocentini et al., 2024).

672 Unlike traditional point-based threshold systems, which are limited in their ability to  
673 account for spatial variability across complex terrain, this approach integrates spatially  
674 continuous thresholds. This design allows the system to address terrain-induced variability in  
675 rainfall-triggered landslides while maintaining computational efficiency for regional-scale  
676 applications (Calvello and Piciullo, 2016; Sun et al., 2024). Moreover, by incorporating  
677 typhoon-specific rainfall parameterization within probabilistic threshold surfaces, this system  
678 significantly advances beyond existing point-based hazard mapping approaches (Guzzetti et  
679 al., 2020; Nolasco-Javier and Kumar, 2018).

680 For effective operational deployment, the system must be integrated with meteorological  
681 monitoring infrastructure, such as weather radar networks and automated rainfall stations.  
682 Critical components of implementation include real-time data processing capabilities,  
683 standardized protocols for disseminating warnings, and post-event validation procedures that  
684 ensure system accuracy and maintain stakeholder trust. The modular design of the system  
685 allows it to be adapted to various regional monitoring networks and institutional frameworks,  
686 making it versatile and scalable across different geographic and organizational contexts.

#### 687 **6.4 Limitations and future research directions**

688 Despite promising advancements, this study has limitations owing to the complexity of  
689 typhoon-induced landslides. First, the model's validation relies solely on landslides from  
690 Typhoon Gaemi. While this single event provided a comprehensive dataset, validating against  
691 multiple, varied typhoons is crucial for model robustness. Typhoons differ significantly in  
692 intensity, rainfall patterns, forward speed, and seasonality, all of which can influence  
693 threshold parameters. For instance, a slow-moving typhoon with higher cumulative rainfall  
694 and lower peak intensity could alter the optimal H24-D7 ratios. Future research should  
695 incorporate landslide inventories from typhoons with contrasting characteristics to assess  
696 threshold transferability and develop adaptive parameterization. The framework's modular  
697 design readily facilitates this by allowing recalibration of the RC24 coefficient for different  
698 typhoon types.

699 Second, the current study primarily addresses rainfall-induced landslides, overlooking  
700 other potential contributing factors. Future work should explore integrating multiple  
701 triggering mechanisms, including earthquakes, human-induced slope modifications, and  
702 typhoon rainfall, for a more comprehensive hazard assessment.

703 Third, the study doesn't explicitly address the potential impacts of climate change on  
704 typhoon rainfall and landslide occurrence. As climate change alters typhoon frequency,

705 intensity, and tracks, future studies should incorporate climate projections specific to  
706 typhoon-prone regions. This will enable the development of forward-looking landslide  
707 warning systems that can adapt to the evolving threats posed by typhoon-specific rainfall.

708 Fourth, while this study demonstrates the effectiveness of ML approaches, further  
709 refinement is possible. Future research should explore advanced deep learning techniques and  
710 ensemble methods to better capture the complex, non-linear relationships between typhoon-  
711 related variables (e.g., rainfall intensity, duration, antecedent moisture) and slope stability.  
712 These advanced methods may offer improved predictive accuracy, more robust uncertainty  
713 quantification, and ultimately, more reliable hazard warnings.

714 Finally, climate projections for Southeast China show a 15–25% increase in peak  
715 typhoon rainfall by 2080 (RCP8.5), which could alter the H24–D7 landslide thresholds from  
716 this study. Higher atmospheric moisture may lower D7 thresholds, while greater rainfall  
717 intensity could require new H24 parameters. Shifting typhoon tracks and seasonality might  
718 also change which areas are vulnerable. Future work must use downscaled climate data to  
719 create non-stationary thresholds, ensuring the long-term reliability of warning systems in the  
720 region.

## 721 **7 Conclusions**

722 This study establishes a novel integrated framework combining optimized LSP with  
723 typhoon-specific rainfall threshold modeling for comprehensive hazard assessment in  
724 mountainous regions. Through systematic analysis of 705 landslides triggered by Typhoon  
725 Gaemi in Zixing City, several key insights emerge:

726 (1) Buffer distance optimization proves critical for typhoon-induced landslide modeling,  
727 with SVM-FR combinations at 0.5-2.0 km distances achieving superior performance (F1-  
728 score: 0.859) compared to conventional approaches. This spatial scale effectively captures

729 typhoon-induced moisture infiltration patterns that differ fundamentally from other triggering  
730 mechanisms.

731 (2) The H24-D7 threshold model demonstrates exceptional stability (71.8% accuracy  
732 across 5-fold validation), successfully characterizing the dual-phase failure mechanism unique  
733 to typhoons: prolonged antecedent saturation coupled with intense precipitation bursts during  
734 typhoon passage.

735 (3) Spatially distributed rainfall thresholds reveal significant heterogeneity, reflecting  
736 complex interactions between typhoon structure and local topography that contradict uniform  
737 regional threshold assumptions in existing operational systems.

738 (4) The integrated warning system achieves operational efficiency through dual-  
739 threshold configuration: H24 thresholds provide immediate response capability during  
740 typhoon landfall, while D7 thresholds enable early detection of vulnerable areas approaching  
741 saturation conditions.

742 (5) This framework addresses three critical gaps in current landslide prediction:  
743 systematic buffer optimization for imbalanced datasets, effective integration of variable  
744 weighting with machine learning algorithms, and development of typhoon-specific spatially  
745 explicit thresholds.

746

747  
748

749 *Code and data availability.* The source code and data will be made available on request.

750 *Competing interests.* The contact author has declared that none of the authors has any  
751 competing interests.

752 *Author contributions.* **Weifeng Xiao:** Writing-review & editing, Validation,  
753 Conceptualization. **Guangchong Yao:** Visualization, Validation, Data curation. **Zhenghui  
754 Xiao:** Writing-review & editing, Formal analysis. **Luguang Luo:** Visualization, Validation,

755 Investigation, Data curation. **Yunjiang Cao**: Visualization, Formal analysis, Data curation.  
756 **Wei Yin**: Validation, Investigation, Correspondence.  
757 *Acknowledgments.* This research was funded by the Research Project on Natural Resources of  
758 Hunan Provincial Department of Natural Resources (No. HBZ20240112), the Open Research  
759 Topic of Hunan Geological Disaster Monitoring Early Warning and Emergency Rescue  
760 Engineering Technology Research Center (No. hndzgczx202409), and the Hunan Provincial  
761 Natural Science Foundation of China (No. 2023JJ30238).

762

763

764

765

## 766 **References**

767 Achu, A. L., Aju, C. D., Pham, Q. B., Reghunath, R., and Anh, D. T.: Landslide susceptibility modeling  
768 using hybrid bivariate statistical - based machine - learning method in a highland segment of Southern  
769 Western Ghats, India, *Environ. Earth Sci.*, 81, 361, <https://doi.org/10.1007/s12665-022-10464-z>, 2022.  
770 Banfi, F. and De Michele, C.: Temporal clustering of precipitation driving landslides over the Italian  
771 Territory, *Earths Future*, 12, e2023EF003885, <https://doi.org/10.1029/2023EF003885>, 2024.  
772 Bogaard, T. and Greco, R.: Hydrological perspectives on precipitation intensity-duration thresholds for  
773 landslide initiation: proposing hydro-meteorological thresholds, *Nat. Hazards Earth Syst. Sci.*, 18, 31–39,  
774 <https://doi.org/10.5194/nhess-18-31-2018>, 2018.  
775 Calvello, M. and Piciullo, L.: Assessing the performance of regional landslide early warning models: the  
776 EDuMaP method, *Nat. Hazards Earth Syst. Sci.*, 16, 103–122, <https://doi.org/10.5194/nhess-16-103-2016>, 2016.  
777 Chang, Z. L., Huang, J. S., Huang, F. M., Bhuyan, K., Meena, S. R., and Catani, F.: Uncertainty analysis of  
779 non-landslide sample selection in landslide susceptibility prediction using slope unit-based machine  
780 learning models, *Gondwana Res.*, 117, 307–320, <https://doi.org/10.1016/j.gr.2023.02.007>, 2023.

781 Cho, W., Park, J., Moon, J., Cha, D. H., Moon, Y. M., Kim, H. S., Noh, K. J., and Park, S. H.: Effects of  
782 topography and sea surface temperature anomalies on heavy rainfall induced by Typhoon Chaba in 2016,  
783 *Geosci. Lett.*, 9, 29, <https://doi.org/10.1186/s40562-022-00230-1>, 2022.

784 Chung, C. C. and Li, Z. Y.: Rapid landslide risk zoning toward multi-slope units of the Neikuihui tribe for  
785 preliminary disaster management, *Nat. Hazards Earth Syst. Sci.*, 22, 1777–1794,  
786 <https://doi.org/10.5194/nhess-22-1777-2022>, 2022.

787 Ciurleo, M., Cascini, L., and Calvello, M.: A comparison of statistical and deterministic methods for  
788 shallow landslide susceptibility zoning in clayey soils, *Eng. Geol.*, 223, 71–81,  
789 <https://doi.org/10.1016/j.enggeo.2017.04.023>, 2017.

790 Dou, H. Q., He, J. B., Huang, S. Y., Jian, W. B., and Guo, C. X.: Influences of non - landslide sample  
791 selection strategies on landslide susceptibility mapping by machine learning, *Geomat. Nat. Haz. Risk*, 14,  
792 1–15, <https://doi.org/10.1080/19475705.2023.2285719>, 2023.

793 Fan, W., Wei, Y. N., and Deng, L. S.: Failure modes and mechanisms of shallow debris landslides using an  
794 artificial rainfall model experiment on Qin-ba Mountain, *Int. J. Geomech.*, 18, 04017157,  
795 [https://doi.org/10.1061/\(ASCE\)GM.1943 - 5622.0001068](https://doi.org/10.1061/(ASCE)GM.1943 - 5622.0001068), 2018.

796 Fan, X. M., Scaringi, G., Korup, O., West, A. J., van Westen, C. J., Tanyas, H., Hovius, N., Hales, T. C.,  
797 Jibson, R. W., Allstadt, K. E., Zhang, L. M., Evans, S. G., Xu, C., Li, G., Pei, X. J., Xu, Q., & Huang, R.  
798 Q. (2019). Earthquake-Induced Chains of Geologic Hazards: Patterns, Mechanisms, and Impacts.  
799 *Reviews of Geophysics*, 57(2), 421-503. <https://doi.org/10.1029/2018RG000626>.

800 Froude, M. J., and Petley, D. N.: Global fatal landslide occurrence from 2004 to 2016, *Nat. Hazards Earth*  
801 *Syst. Sci.*, 18, 2161–2181, <https://doi.org/10.5194/nhess - 18 - 2161 - 2018>, 2018.

802 Gariano, S. L., Brunetti, M. T., Iovine, G., Melillo, M., Peruccacci, S., Terranova, O., Vennari, C., and  
803 Guzzetti, F.: Calibration and validation of rainfall thresholds for shallow landslide forecasting in Sicily,  
804 southern Italy, *Geomorphology*, 228, 653–665, <https://doi.org/10.1016/j.geomorph.2014.10.019>, 2015.

805 Gariano, S. L., and Guzzetti, F.: Landslides in a changing climate, *Earth - Sci. Rev.*, 162, 227–252,  
806 <https://doi.org/10.1016/j.earscirev.2016.08.011>, 2016.

807 Guo, W. X., Ye, J., Liu, C. B., Lv, Y. J., Zeng, Q. Y., and Huang, X.: An approach for predicting landslide  
808 susceptibility and evaluating predisposing factors, *Int. J. Appl. Earth Obs.*, 135, 104217,  
809 <https://doi.org/10.1016/j.jag.2024.104217>, 2024.

810 Guzzetti, F., Gariano, S. L., Peruccacci, S., Brunetti, M. T., Marchesini, I., Rossi, M., and Melillo, M.:  
811 Geographical landslide early warning systems, *Earth - Sci. Rev.*, 200, 102973,  
812 <https://doi.org/10.1016/j.earscirev.2019.102973>, 2020.

813 Guzzetti, F.: Invited perspectives: Landslide populations - can they be predicted?, *Nat. Hazards Earth Syst.*  
814 *Sci.*, 21, 1467–1471, <https://doi.org/10.5194/nhess-21-1467-2021>, 2021.

815 Huang, F., Chen, J., Liu, W., Huang, J., Hong, H., and Chen, W.: Regional rainfall - induced landslide  
816 hazard warning based on landslide susceptibility mapping and a critical rainfall threshold,  
817 *Geomorphology*, 408, 108236, <https://doi.org/10.1016/j.geomorph.2022.108236>, 2022.

818 Huang, Y., and Zhao, L.: Review on landslide susceptibility mapping using support vector machines,  
819 *Catena*, 165, 520–529, <https://doi.org/10.1016/j.catena.2018.03.003>, 2018.

820 Kalantar, B., Pradhan, B., Naghibi, S. A., Motevalli, A., and Mansor, S.: Assessment of the effects of  
821 training data selection on the landslide susceptibility mapping: A comparison between support vector  
822 machine (SVM), logistic regression (LR), and artificial neural networks (ANN), *Geomat. Nat. Haz. Risk*,  
823 9, 49–69, <https://doi.org/10.1080/19475705.2017.1407368>, 2018.

824 Kenanoglu, M. B., Ahmadi - Adli, M., Toker, N. K., and Huvaj, N.: Effect of unsaturated soil properties on  
825 the intensity-duration threshold for rainfall triggered landslides, *Tek. Dergi*, 30, 9009–9027,  
826 <https://doi.org/10.18400/tekderg.414884>, 2019.

827 Kirschbaum, D. and Stanley, T.: Satellite-Based Assessment of Rainfall-Triggered Landslide Hazard for  
828 Situational Awareness, *Earth's Future*, 6, 505–523, <https://doi.org/10.1002/2017EF000715>, 2018.

829 Lee, J. T., Ko, K. Y., Lee, D. I., You, C. H., and Liou, Y. C.: Enhancement of orographic precipitation in  
830 Jeju Island during the passage of Typhoon Khanun (2012), *Atmos. Res.*, 201, 58–71,  
831 <https://doi.org/10.1016/j.atmosres.2017.10.013>, 2018.

832 Li, Y. L., Lin, Y. L., and Wang, Y. Q.: A numerical study on the formation and maintenance of a long -  
833 lived rainband in Typhoon Longwang (2005), *J. Geophys. Res. Atmos.*, 124(19), 10401–10426,  
834 <https://doi.org/10.1029/2019JD030600>, 2019.

835 Liu, L. L., Zhang, Y. L., Xiao, T., and Yang, C.: A frequency ratio - based sampling strategy for landslide  
836 susceptibility assessment, *Bull. Eng. Geol. Environ.*, 81, 360, <https://doi.org/10.1007/s10064-022-02836-3>, 2022.

838 Liu, M. F., Vecchi, G. A., Smith, J. A., and Murakami, H.: The present-day simulation and Twenty-First-  
839 Century Projection of the Climatology of Extratropical Transition in the North Atlantic, *J. Climate*, 30,  
840 2739–2756, <https://doi.org/10.1175/JCLI-D-16-0352.1>, 2017.

841 Lombardo, L., and Mai, P. M.: Presenting logistic regression - based landslide susceptibility results, *Eng.*  
842 *Geol.*, 244, 14–24, <https://doi.org/10.1016/j.enggeo.2018.07.019>, 2018.

843 Ma, H., Wang, F. W., Fu, Z. J., Feng, Y. Q., You, Q., and Li, S.: Characterizing the clustered landslides  
844 triggered by extreme rainfall during the 2024 typhoon Gaemi in Zixing City, Hunan Province, China,  
845 *Landslides*, 22, 2311–2329, <https://doi.org/10.1007/s10346-025-02510-1>, 2025.

846 Merghadi, A., Yunus, A. P., Dou, J., Whiteley, J., ThaiPham, B., Bui, D. T., Avtar, R., and Abderrahmane,  
847 B.: Machine learning methods for landslide susceptibility studies: A comparative overview of algorithm  
848 performance, *Earth-Sci. Rev.*, 207, 103225, <https://doi.org/10.1016/j.earscirev.2020.103225>, 2020.

849 Mirus, B. B., Becker, R. E., Baum, R. L., and Smith, J. B.: Integrating real-time subsurface hydrologic  
850 monitoring with empirical rainfall thresholds to improve landslide early warning, *Landslides*, 15, 1909–  
851 1919, <https://doi.org/10.1007/s10346-018-0995-z>, 2018.

852 Mondini, A. C., Guzzetti, F., and Melillo, M.: Deep learning forecast of rainfall-induced shallow landslides,  
853 *Nat. Commun.*, 14, 10.1038/s41467-023-38135-y, <https://doi.org/10.1038/s41467-023-38135-y>, 2023.

854 Niu, H. T., Shao, S. J., Gao, J. Q., and Jing, H.: Research on GIS-based information value model for  
855 landslide geological hazards prediction in soil - rock contact zone in southern Shaanxi, *Phys. Chem.*  
856 *Earth*, 133, 103515, <https://doi.org/10.1016/j.pce.2023.103515>, 2024.

857 Nocentini, N., Medici, C., Barbadori, F., Gatto, A., Franceschini, R., del Soldato, M., Rosi, A., and Segoni,  
858 S.: Optimization of rainfall thresholds for landslide early warning through false alarm reduction and a  
859 multi-source validation, *Landslides*, 21, 557–571, <https://doi.org/10.1007/s10346-023-02176-7>, 2024.

860 Nolasco-Javier, D. and Kumar, L.: Deriving the rainfall threshold for shallow landslide early warning  
861 during tropical cyclones: a case study in northern Philippines, *Nat. Hazards*, 90, 921–941,  
862 <https://doi.org/10.1007/s11069-017-3081-2>, 2018.

863 Panchal, S., and Shrivastava, A. K.: A comparative study of frequency ratio, Shannon's entropy and  
864 analytic hierarchy process (AHP) models for landslide susceptibility assessment, *ISPRS Int. J. Geo-Inf.*,  
865 10, 603, <https://doi.org/10.3390/ijgi10090603>, 2021.

866 Piciullo, L., Calvello, M., and Cepeda, J. M.: Territorial early warning systems for rainfall - induced  
867 landslides, *Earth-Sci. Rev.*, 179, 228–247, <https://doi.org/10.1016/j.earscirev.2018.02.013>, 2018.

868 Piciullo, L., Gariano, S. L., Melillo, M., Brunetti, M. T., Peruccacci, S., Guzzetti, F., and Calvello, M.:  
869 Definition and performance of a threshold - based regional early warning model for rainfall - induced  
870 landslides, *Landslides*, 14, 995–1008, <https://doi.org/10.1007/s10346-016-0750-2>, 2017.

871 Regmi, N. R., Walter, J. I., Jiang, J. L., Orban, A. M., and Hayman, N. W.: Spatial patterns of landslides in  
872 a modest topography of the Ozark and Ouachita Mountains, USA, *Catena*, 245, 108344,  
873 <https://doi.org/10.1016/j.catena.2024.108344>, 2024.

874 Reichenbach, P., Rossi, M., Malamud, B. D., Mihir, M., and Guzzetti, F.: A review of statistically - based  
875 landslide susceptibility models, *Earth-Sci. Rev.*, 180, 60–91,  
876 <https://doi.org/10.1016/j.earscirev.2018.03.001>, 2018.

877 Sahin, E. K.: Comparative analysis of gradient boosting algorithms for landslide susceptibility mapping,  
878 *Geocarto Int.*, 37, 2441–2465, <https://doi.org/10.1080/10106049.2020.1831623>, 2022.

879 San, B. T.: An evaluation of SVM using polygon-based random sampling in landslide susceptibility  
880 mapping: The Candir catchment area (western Antalya, Turkey), *Int. J. Appl. Earth Obs.*, 26, 399–412,  
881 <https://doi.org/10.1016/j.jag.2013.09.010>, 2014.

882 Segoni, S., Lagomarsino, D., Fanti, R., Moretti, S., and Casagli, N.: Integration of rainfall thresholds and  
883 susceptibility maps in the Emilia Romagna (Italy) regional - scale landslide warning system, *Landslides*,  
884 12, 773–785, <https://doi.org/10.1007/s10346-014-0502-0>, 2015.

885 Segoni, S., Piciullo, L., and Gariano, S. L.: A review of the recent literature on rainfall thresholds for  
886 landslide occurrence, *Landslides*, 15, 1483–1501, <https://doi.org/10.1007/s10346-018-0966-4>, 2018a.

887 Segoni, S., Rosi, A., Lagomarsino, D., Fanti, R., and Casagli, N.: Brief communication: Using averaged  
888 soil moisture estimates to improve the performances of a regional - scale landslide early warning system,  
889 *Nat. Hazards Earth Syst. Sci.*, 18, 807–812, <https://doi.org/10.5194/nhess-18-807-2018>, 2018b.

890 Steger, S., Brenning, A., Bell, R., and Glade, T.: The propagation of inventory - based positional errors into  
891 statistical landslide susceptibility models, *Nat. Hazards Earth Syst. Sci.*, 16, 2729–2745,  
892 <https://doi.org/10.5194/nhess-16-2729-2016>, 2016.

893 Sun, D. L., Wu, X. Q., Wen, H. J., and Gu, Q. Y.: A LightGBM-based landslide susceptibility model  
894 considering the uncertainty of non-landslide samples, *Geomat. Nat. Haz. Risk*, 14, 2213807,  
895 <https://doi.org/10.1080/19475705.2023.2213807>, 2023.

896 Sun, Y., Zhang, J., Wang, H. A., and Lu, D. G.: Probabilistic thresholds for regional rainfall induced  
897 landslides, *Comput. Geotech.*, 166, 106040, <https://doi.org/10.1016/j.compgeo.2023.106040>, 2024.

898 Thiene, M., Shaw, W. D., and Scarpa, R.: Perceived risks of mountain landslides in Italy: Stated choices for  
899 subjective risk reductions, *Landslides*, 14, 1077–1089, <https://doi.org/10.1007/s10346-016-0741-3>, 2017.

900 Tufano, R., Formetta, G., Calcaterra, D., and De Vita, P.: Hydrological control of soil thickness spatial  
901 variability on the initiation of rainfall-induced shallow landslides using a three - dimensional model,  
902 *Landslides*, 18, 3367–3380, <https://doi.org/10.1007/s10346-021-01681 - x>, 2021.

903 Xiao, W. F., Zhou, Z. Y., Ren, B. Z., and Deng, X. P.: Integrating spatial clustering and multi - source  
904 geospatial data for comprehensive geological hazard modeling in Hunan Province, *Sci. Rep.*, 15, 1982,  
905 <https://doi.org/10.1038/s41598-024-84825 - y>, 2025.

906 Yan, F., Zhang, Q. W., Ye, S., and Ren, B.: A novel hybrid approach for landslide susceptibility mapping  
907 integrating analytical hierarchy process and normalized frequency ratio methods with the cloud model,  
908 *Geomorphology*, 327, 170–187, <https://doi.org/10.1016/j.geomorph.2018.10.024>, 2019.

909 Yang, C., Liu, L. L., Huang, F. M., Huang, L., and Wang, X. M.: Machine learning - based landslide  
910 susceptibility assessment with optimized ratio of landslide to non-landslide samples, *Gondwana Res.*,  
911 123, 198–216, <https://doi.org/10.1016/j.gr.2022.05.012>, 2023.

912 Yang, K. H., Uzuoka, R., Thuo, J. N., Lin, G. L., and Nakai, Y.: Coupled hydro-mechanical analysis of two  
913 unstable unsaturated slopes subject to rainfall infiltration, *Eng. Geol.*, 216, 13–30,  
914 <https://doi.org/10.1016/j.enggeo.2016.11.006>, 2017.

915 Zêzere, J. L., Pereira, S., Melo, R., Oliveira, S. C., and Garcia, R. A. C.: Mapping landslide susceptibility  
916 using data-driven methods, *Sci. Total Environ.*, 589, 250–267,  
917 <https://doi.org/10.1016/j.scitotenv.2017.02.188>, 2017.

918 Zhao, Z., Liu, Z. Y., and Xu, C.: Slope unit-based landslide susceptibility mapping using certainty factor,  
919 support vector machine, random forest, CF-SVM and CF-RF models, *Front. Earth Sci.*, 9, 589630,  
920 <https://doi.org/10.3389/feart.2021.589630>, 2021.

921 Zou, Y., Wei, Z. F., Zhan, Q. M., and Zhou, H. J.: An extreme storm over the Nanling Mountains during  
922 Typhoon Bilis and the roles of terrain, *Nat. Hazards*, 116, 795–815, <https://doi.org/10.1007/s11069-022-05699-9>, 2023.